Mechanical Systems and Signal Processing 134 (2019) 106335

Contents lists available at ScienceDirect

Mechanical Systems and Signal Processing

journal homepage: www.elsevier.com/locate/ymssp

Position control based on the estimated bending force in a soft robot with tunable stiffness

Junfeng Li

School of Mechanical and Electronic Engineering, Wuhan University of Technology, 122 Luoshi Road, Wuhan, Hubei 430070, China

ARTICLE INFO

Article history:
Received 27 March 2019
Received in revised form 29 May 2019
Accepted 29 August 2019

Keywords:
Position control
Tunable stiffness
Self-sensing method
Soft robot
SMA

ABSTRACT

In this paper, a control method based on the predicted bending force is proposed to increase the position-tracking accuracy of a soft robot when the stiffness is adjusted in open- and closed-loop control systems. For the open-loop stiffness-control system, the predicted bending force and stiffness of the soft robot are modeled, including the major and minor hysteresis effects. For the closed-loop stiffness-control system, a self-sensing method based on resistance is used to represent the stiffness, which cannot be measured directly by the sensor. Then, the bending force of the soft robot can be estimated from the measured resistance. The experimental results show that the proposed method leads to more accurate and robust tracking-control performance than time delay estimation (TDE) when the stiffness changes because the input voltage based on the estimated bending force for the SMA-2 can be properly calculated once the stiffness of the soft robot is changed. This paper proposes a feasible method to simultaneously control the stiffness (based on the self-sensing method) and position, resulting in more accurate tracking performance than the TDE approach without the predicted bending force.

1. Introduction

Bioinspiration has led to the construction of many soft robots that have infinite degrees of freedom due to their inherently compliant and articulate characteristics. These robots can perform a variety of tasks, such as dexterous manipulation in constrained environments and safe grasping with soft contact [1,2]. However, these soft robots have inherent disadvantages, such as the lack of a variable stiffness mechanism that can adapt to various environments.

Recently, particle-jamming technologies and certain materials (such as fusible alloys) have been used to achieve variable stiffness actuation for soft robots [3,4]; these variable stiffness methods dramatically increase robot adaptability to new environments. However, these variable stiffness systems either increase the complexity and weight of the soft robot or have long activation timescales that are not ideal for practical environments. Furthermore, these works primarily focus exclusively on robot stiffness control without simultaneously considering position control.

Relative to electric, hydraulic, and pneumatic actuators, shape-memory alloy (SMA) actuators have a high power-to-weight ratio, low driving voltages, low cost, and silent operation, making them suitable for a wide variety of applications [5,6]. In this paper, we use the same prototype of soft robot as in our previous research [7]. As shown in Fig. 1, three types of SMA wires, termed SMA-1, SMA-2 and SMA-3, are embedded in a soft robot. SMA-1 is used as the bone structure to support the soft robot. To actuate the soft robot, one SMA-2 fiber is used for large contractions because of its low strain; it is

E-mail address: jflichina@whut.edu.cn

https://doi.org/10.1016/j.ymssp.2019.106335
0888-3270/

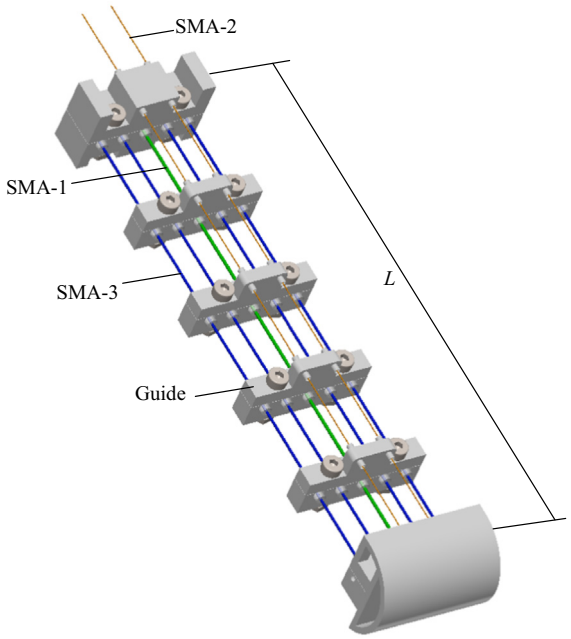

Fig. 1. The overall mechanical structure of the soft robot.

placed into the soft robot in a *U* shape to double its driving capacity. The stiffness of the soft robot is changed when the four SMA-3 wires are heated; these wires have a memorized straight-line shape that does not change in length when heated from the martensite phase to the austenite phase. The guides of the structure were manufactured using a 3D printer. The mechanical parameters of the soft robot are shown in Table 1. Reference [7] contains detailed information about the soft robot.

Due to the hysteresis effect arising from the nonlinearities of SMAs, it is difficult to achieve accurate position tracking control. Many hysteresis-model-free schemes have been developed to compensate for the nonlinearities and parametric uncertainties of the SMA. Time delay control (TDC) has good performance using time delay estimation (TDE) to compensate for the nonlinear dynamics and disturbances with time-delayed signals [8]. TDC a has compact structure and a relatively simple gain-selection procedure and is robust against modeling error, parameter variation, and disturbances since it does not require a system model or a disturbance model. Therefore, TDC has been successfully applied to many applications over the past decades, such as position tracking and impedance control [9]. However, TDC demonstrates an inherent performance

Table 1
Mechanical parameters of the soft robot.

SMA-1	Young's modulus E_1	56 GPa
	Length L_1	100 mm
	Diameter d_1	0.6 mm
	Moment of inertia constant I_1	6.359×10^{-3} mm^4
SMA-2	Diameter d_2	0.15 mm
	Length L_2	600 mm
SMA-3	Young's modulus in martensite phases E_M	25 GPa
	Young's modulus in austenite phases E_A	44 GPa
	Diameter d_3	0.5 mm
	Length L_3	100 mm
	Initial strain	0 mm
	Density ρ	6.5×10^{12} kg/mm^3
	Moment of inertia constant I_3	3.066×10^{-3} mm^4
	Austenite start (A_s)	26.7 °C
	Austenite final (A_f)	45 °C
	Martensite start (M_s)	39 °C
	Martensite final (M_f)	25.5 °C
Robot	l_{SMA}	4.5 mm
	Length L	100 mm
	l_d	20 mm
	d	8 mm

limitation incurred by TDE error since the continuous-time closed-loop dynamics is approximated in a discrete form, which affects both the stability and performance of closed-loop systems.

Control of an SMA-actuated soft robot has been a challenge, especially when its stiffness is changed. To increase the position-tracking accuracy and robustness of an SMA, a novel control method based on radial basis function (RBF) neural networks and estimated bending force is proposed in this paper to achieve accurate position-tracking control when the stiffness is changed simultaneously with position. The topic of this study is the development of control methods to reduce position-tracking errors caused by tunable stiffness in a soft robot actuated by SMAs. The contributions of this paper are as follows: (1) a self-sensing method based on resistance is used to represent the tunable stiffness, and (2) accurate position-tracking control is achieved for both open- and closed-loop stiffness-control systems based on the estimated bending force.

2. Modeling and testing the variable stiffness capability of the soft robot

In this section, the stiffness of the soft robot, which is adjusted by heating the SMA-3, is modeled and tested. To model the soft robot, the assumptions are as follows: (1) SMA-1 and SMA-3 are flexible incompressible rods, and the soft robot bends into an arc shape with a constant curvature, (2) the ambient temperature remains unchanged, and (3) the variable stiffness mechanism can be treated as a three-element system in which thermal energy is converted into a phase transformation and then into mechanical work. The heat for the phase transformation is generated by applying a current to the SMA-3, and the heat-energy balance governs its temperature. A thermal model is formulated to describe the rate of temperature change due to a change in the current of the wire and the convective heat loss to the environment; it is given by the first-order dynamic equation:

$$0.25\rho c(T)\pi L_3 d_3^2 \dot{T} = i_{SMA-3}^2 R_3 - h(T)A(T - T_{amb}) \tag{1}$$

where ρ is the mass density of SMA-3, T is its temperature and $\dot{T}=dT/dt$; i_{SMA-3} is the current applied to SMA-3; A is its circumferential area; T_{amb} is the ambient temperature; R_3 is the resistance of the SMA-3 wire; and $h(T)$ and $c(T)$ are the convection heat-transfer coefficient and specific heat of the SMA-3, respectively, which can be expressed by [9]:

$$h(T) = \begin{cases} a_1 - a_2 T & \dot{T} \geq 0 \\ a_3 + a_4 \mathrm{erf}[(T - a_5)/a_6]) & \dot{T} < 0 \end{cases} \tag{2}$$

$$c(T) = \begin{cases} b_1 + b_2 \mathrm{erf}[(T - b_3)/b_4]) & \dot{T} \geq 0 \\ b_5 T_{max} - b_6 & \dot{T} < 0 \end{cases} \tag{3}$$

Here, a_j and b_j with subscripts j are constant parameters, and T_{max} is the maximum temperature before cooling.

SMAs have an inherent hysteresis during the transformation between their martensite and austenite phases. The martensite fraction ξ of the SMA materials can be calculated as a function of stress and the temperature during heating ($\dot{T} \geq 0$) or cooling ($\dot{T} < 0$) transformations, which can be expressed by [8]:

$$\xi_{heating} = 0.5\xi_M \cos[a_A(T - A_s) + b_A\sigma] + 0.5\xi_M, \quad A_s + \sigma/C_A \leq T \leq A_f + \sigma/C_A \tag{4}$$

$$\xi_{cooling} = 0.5(1 - \xi_A)\cos[a_M(T - M_f) + b_M\sigma] + 0.5(1 + \xi_A), \quad M_s + \sigma/C_M \leq T \leq M_f + \sigma/C_M \tag{5}$$

where ξ_M and ξ_A are the initial martensite fractions for each transformation, C_A and C_M are constant material coefficients that can describe the temperature and the critical stress to induce the transformation, and σ is the stress of the SMA-3. A_f, A_s, M_s and M_f are the phase transformation temperatures listed in Table 1. a_A, a_M, b_A and b_M are the material properties, which can be expressed by:

$$\begin{cases} a_A = \pi/(A_f - A_s), \quad a_M = \pi/(M_s - M_f) \\ b_A = -a_A/C_A, \quad b_M = -a_M/C_M \end{cases} \tag{6}$$

In this paper, a_A and a_M are set to 0.17 and 0.23, respectively. As there is no pretension applied to the SMA-3 during heating and cooling, $b_A\sigma = b_M\sigma = 0$.

The constitutive model of SMA shows the relationship between the stress rate $\dot{\sigma}$, strain rate $\dot{\varepsilon}$, temperature rate $\dot{T}$ and martensite volumetric fraction rate $\dot{\xi}$, which can be defined as:

$$\dot{\sigma} = E\dot{\varepsilon} + \Theta\dot{T} + \Omega\dot{\xi} \tag{7}$$

where E represents the Young modulus, Θ corresponds to the thermal expansion factor, and Ω is the phase transformation factor. Eq. (7) shows that the relationship between E and T is hysteretic. To simplify this relationship, the Young's modulus E_3 and resistance R_3 of the SMA-3 wire can be given by:

$$E_3 = \xi E_M + (1 - \xi)E_A \tag{8}$$

$$R_3 = \xi R_M + (1-\xi)R_A \tag{9}$$

where E_Φ or R_Φ with subscripted numbers $\Phi \in \{M, A\}$ are the constant parameters corresponding to the martensite and austenite phases, respectively.

Constant curvature has often been viewed as a desirable characteristic in soft robots due to the associated simplifications in kinematic modeling, which has been successfully applied to many soft robots [9]. Fig. 2(a) shows the experiment setup for the variable stiffness test. F_d will be measured by the load cell at three different bending angles ($\beta = 30°$, 60°, and 90°) when the SMA-3 is heated with a power supply. Fig. 2(b) shows the bending configuration of the soft robot and the relationship between bending force F_d and bending angle, which can be expressed by [10]:

$$F_d = \beta\, S_b/(Ld) = \beta\,(E_1 I_1 + 4E_3 I_3)/(Ld) \quad 0 \le \beta \le 2\pi \tag{10}$$

where I_1 and I_3 are the moment of inertia constants of SMA-1 and SMA-3, respectively, E_1 is the Young modulus of SMA-1, L is the length of the soft robot, and d is the lever of pulling force; the bending stiffness S_b changes when SMA-3 is heated by current. Then, in theory, the maximum and minimum values of the soft robot's stiffness are $S_{b-min} = 662 \times 10^{-6}$ Nm^2 and $S_{b-max} = 895 \times 10^{-6}$ Nm^2, respectively. Details of the parameters are provided in Tables 1 and 2.

To obtain a quick response for variable stiffness, the heating current is set as an "on-off" binary control (first heating, then cooling) with various values. In addition, the martensite starting temperature of the minor hysteresis effect must be identified when the phase transformation of SMA-3 from martensite to austenite is not fully complete with the small heating current, which satisfies the experimental results:

$$M_{s-minor} = f(\xi) + M_s \tag{11}$$

where $f(\xi) = g_4\xi^4 + g_3\xi^3 + g_2\xi^2 + g_1\xi + g_0$ is the modified function of the martensite start temperature for the minor hysteresis effect; g_j with subscripts j are the fitting parameters. Fig. 2(c) illustrates the working space of the soft robot. As the maximum output displacement of SMA-2 is less than 30 mm, the maximum bending position x for the experimental tests of the soft robot was set to 70 mm.

Fig. 3(a) and (b) show the simulation temperature and martensite fraction ξ of the SMA-3 corresponding to the various "on-off" input currents (heating from 10 s to 30 s and cooling from 30 s to 115 s). Fig. 3(c–e) show that the simulated F_d (solid lines) derived from Eqs. (1)–(11) for various bending shapes agree qualitatively with the experimental results (dashed

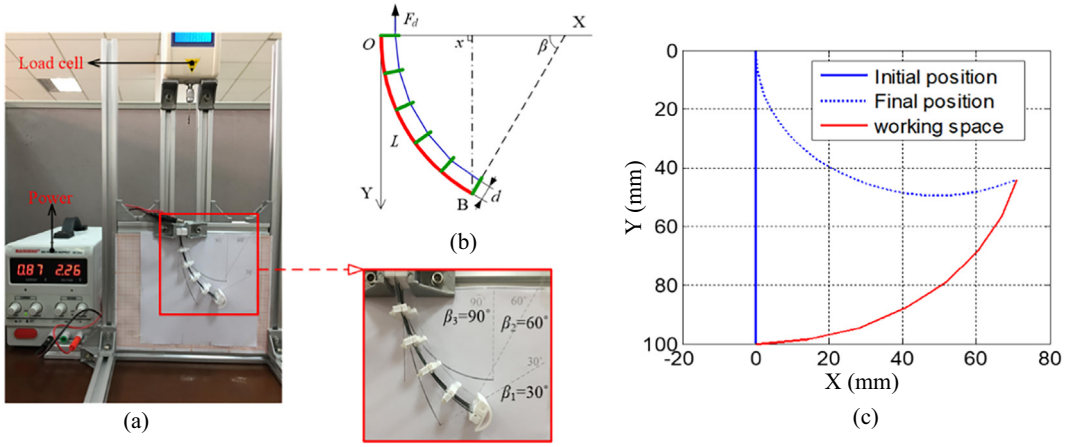

Fig. 2. Analysis of bend shape for the soft robot. (a) Experimental setup; (b) bending configuration of the soft robot; and (c) working space.

Table 2
Parameters for the simulation.

a_1	280	b_1	2300
a_2	0.5	b_2	100
a_3	250	b_3	38
a_4	260	b_4	5
a_5	48	b_5	30.5
a_6	20	b_6	526
R_M	4.013 Ω	T_{amb}	25 °C
R_A	3.551 Ω	g_2	17.2
g_4	21.8	g_1	2.5
g_3	−32.6	g_0	1.9

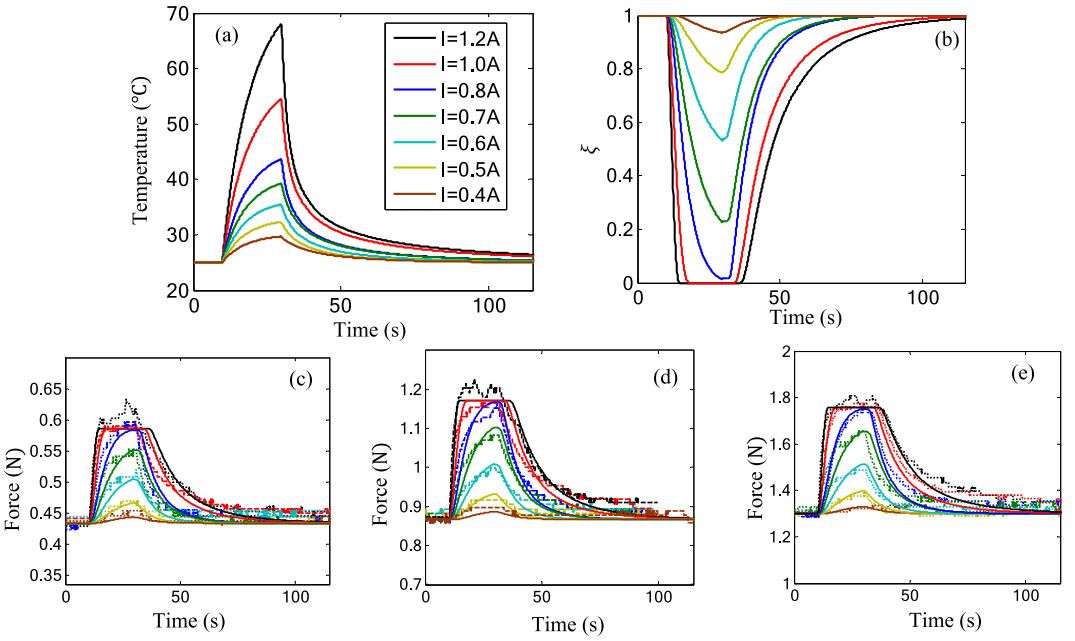

Fig. 3. Simulation and experimental results for the variable stiffness mechanism. The simulation temperature under various input currents; (b) the martensite fraction ξ of the SMA-3; (c–e) the simulated and experimental F_d values corresponding to bending positions $\beta = 30°$, 60°, and 90°, respectively.

lines), including the major (heating current i_{SMA-3} = 1.2 A and 1.0 A) and minor (heating current i_{SMA-3} = 0.8 A, 0.7 A, 0.6 A, 0.5 A, and 0.4 A) hysteresis effects. Details of the parameters of the simulation are listed in Table 2.

3. Position tracking with open-loop control of stiffness

3.1. Control method design

Instead of controlling only the bending position of the soft robots, this paper attempts to simultaneously control both the position and stiffness of the SMA-actuated soft robot. Due to the nonlinear saturated hysteretic behavior of SMA during phase transformations, it is not easy to achieve accurate position-tracking control by establishing an effective controller for the soft robot.

To reduce the hysteresis problem of the SMA actuators, several methods based on device design [11] and model-free schemes have been developed [9]. The RBF neural network is one of the most widely used models in nonlinear control systems, having simpler structures, faster training speeds and stronger generalizability than other types of neural networks [12–15]. In this paper, as shown in Fig. 4, the position-control strategy of the soft robot can be divided into two parts. Part I shows the three-element variable stiffness mechanism, which can be expressed with Eqs. (1)–(11). Part II shows the position-control strategy based on RBF compensation and estimated bending force according to the stiffness of the soft robot.

As shown in Fig. 2(b), the tip's position B in the X direction can be expressed by:

$$x = f_1(\beta) = 2\pi\chi(1 - cos\ \beta) \tag{12}$$

where $\chi = L/\beta$ is the bending radius. In addition, because it is difficult to obtain the inverse model $\beta = f_1^{-1}(x)$, the bending angle β can be expressed by:

$$\beta = p_3x^3 + p_2x^2 + p_1x + p_0 \tag{13}$$

where the p_j with subscripted numbers j are fitting parameters.

Then, F_d can be predicted relative to reference position x with Eqs. (10)–(13) when the stiffness is changed. Furthermore, input voltage V_{SMA-2} can be chosen and used to bend the soft robot if the relationship between V_{SMA-2} and F_d of the SMA-2 is established. As shown in Fig. 5, the red and black lines represent the inverse model of the input voltage and output force of SMA-2 during heating and cooling, respectively. The input voltage for heating ($V_{SMA-2(h)}$) and cooling ($V_{SMA-2(c)}$) can be modeled as:

$$\begin{cases} V_{SMA-2(h)} = n_1 + n_2 \times (F_d - n_3)^3 \\ V_{SMA-2(c)} = m_1 + m_2 \times (F_d - m_3)^3 \end{cases} \tag{14}$$

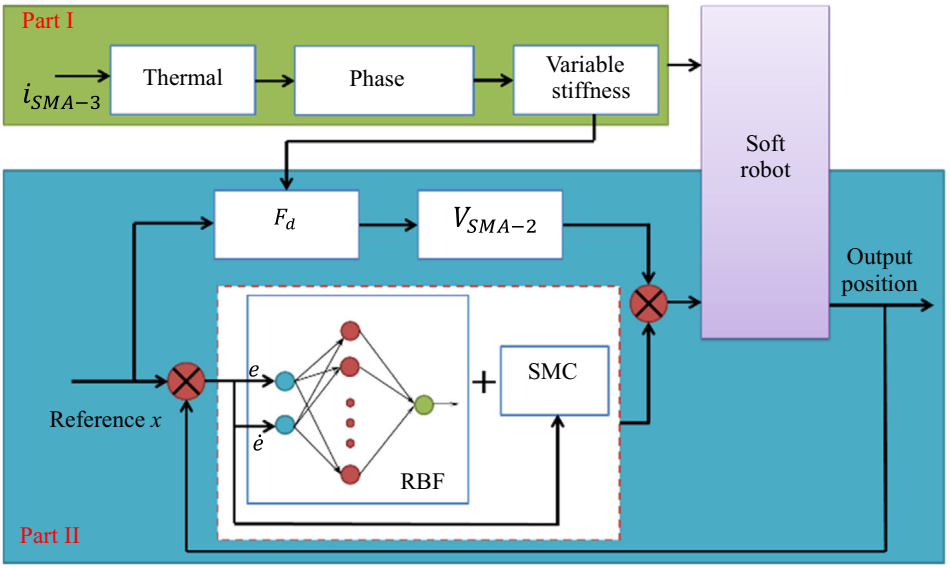

Fig. 4. Position-control strategy of the soft robot with open-loop stiffness control. Part I is the open-loop control of stiffness; Part II is the position control.

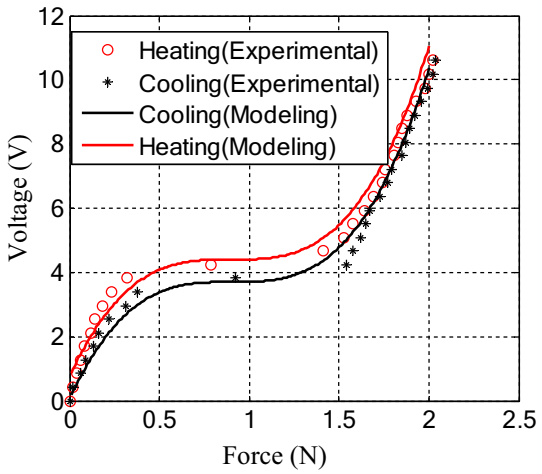

Fig. 5. The inverse model of input voltage and output force for SMA-2.

where n_j and m_j with subscripts j are constant parameters.

Because F_d is related to i_{SMA-3} according to Eqs. (1)–(10), the input voltage $V_{SMA-2} = f_2(x, i_{SMA-3}, F_d)$ of SMA-2 can be derived from the tip position$x$ and input current i_{SMA-3}. Since the RBF neural network (consisting of three inner layers: an input layer, a hidden layer and a linear output layer) provides excellent approximations for uncertainties caused by nonlinear systems and disturbances, it can be used to approximate the input uncertainty for SMA-2 that is assumed to be bounded. The total input voltage is rewritten as:

$$V_{SMA-2} = f_2(x, i_{SMA-3}, F_d) + \psi u_{RBF} \tag{15}$$

where $|\psi u_{RBF}| \le \aleph_1$ is bounded; $\aleph_1$ denotes a positive value. ψ is the coefficient, and u_{RBF} is the output of the RBF neural network, which can also be given as [10]:

$$\begin{cases} u_{RBF}(k) = W^T(k)H(k) \\ W^T(k) = [w_1(k),\ w_2(k),\ w_3(k), \cdots,\ w_n(k)] \\ H(k) = [h_1(k),\ h_2(k),\ h_3(k), \cdots,\ h_n(k)]^T \end{cases} \tag{16}$$

Here, $W^T(k)H(k)$ is the linear output layer, n is the number of hidden-layer neurons, $w_n(k)$ is a hidden-layer-to-output interconnection weight, and $h_n(k)$ is the hidden layer with the RBF activation function, which can be expressed as:

$$h_n(k) = exp\left\{-\frac{\|X(k) - D_n(k)\|}{2\sigma_n(k)^2}\right\} \tag{17}$$

where $X(k)$ is a vector of the input layer for the network. $\|\cdot\|$ denotes the Euclidean norm, $D_n(k)$ is a vector of the center, and $\sigma_n(k)$ is the width. For simplicity, the centers and widths are predefined and fixed. Therefore, $D_n(1) = D_n(2), \cdots, = D_n(k)$ and $\sigma_n(1) = \sigma_n(2), \cdots, = \sigma_n(k)$. In this paper, the input layer $X(k)$ and vector of center $D_n(k)$ can be expressed as:

$$X(k) = [e(k),\ \dot{e}(k)]^T \tag{18}$$

$$D_n(k) = [D_{n1}(k),\ D_{n2}(k)]^T \tag{19}$$

where $e(k) = x(k) - x_d(k)$ and $\dot{e}(k) = [e(k) - e(k-1)]/dt$. dt is the sampling time of microcontroller, and $x(k)$ and $x_d(k)$ are the actual and desired inputs, respectively.

To achieve fast and accurate position-tracking performance for the soft robot, a sliding mode controller (SMC) is needed, and Eq. (15) can be rewritten as:

$$V_{SMA-2} = f_2(x, i_{SMA-3}, F_d) + \psi(u_{RBF} + u_{SMC}) \tag{20}$$

Here, u_{SMC} is the SMC output, which can be expressed as:

$$u_{SMC} = qs(k) + \epsilon\ sign[s(k)/\delta] \tag{21}$$

where q, ϵ and δ are tunable parameters to guarantee stability and $s(k)$ is a sliding surface.

Concerning the SMC, the sliding surface is defined as:

$$s(k) = ce(k) + \dot{e}(k), \quad c > 0 \tag{22}$$

where c denotes the design value.

Finally, combining Eqs. (16), (17), (20), and (21), the control law based on SMC and the RBF neural networks is expressed by:

$$V_{SMA-2} = f_2(x, i_{SMA-3}, F_d) + \psi\ W^T(k)H(k) + \psi\ q(ce(k) + \dot{e}(k)) + \psi\ \epsilon sign\{[ce(k) + \dot{e}(k)]/\delta\} \tag{23}$$

To ensure that the final output of the network gradually approximates the nonlinear dynamic system in Eq. (15) and the tracking error approaches zero along the sliding surface when $t \to \infty$, the weight connections between the hidden layer and the output layer need to be updated as follows:

$$\dot{W}(k) = \alpha s(k)H(k) \tag{24}$$

where α is the learning rate.

Table 3
Parameters for the RBF compensation and TDE.

p_3	0.1×10^{-3}	p_1	1.277
p_2	-0.70×10^{-2}	p_0	−0.533
n_1	4.4	m_1	3.7
n_2	5	m_2	5
n	9	$\sigma_{1,\cdots,9}$	35
ψ	1.458×10^{-2}	D_5	$[0\ ,\ 0]^T$
D_1	$[-5\ ,-5]^T$	D_6	$[0.5\ ,0.5]^T$
D_2	$[-2.5\ ,-2.5]^T$	D_7	$[1\ ,1]^T$
D_3	$[-1\ ,-1]^T$	D_8	$[2.5\ ,2.5]^T$
D_4	$[-0.5\ ,-0.5]^T$	D_9	$[5\ ,5]^T$
δ	4	q	3.7
$\in$	0.01	c	5
α	0.01	B	2.2×10^{-2}
λ	0.5	ζ	0.2
V_{max}	2.32 V	V_{min}	2.66V
N_1	9.5	N_2	1.55
z_{h3}	77.77	z_{h2}	-7.66×10^2
z_{h1}	2.416×10^3	z_{h0}	-2.354×10^3
z_{c3}	-2.464×10^2	z_{h2}	2.985×10^3
z_{c1}	-1.204×10^4	z_{h0}	1.619×10^4
c_1	0.21	q_1	0.05
$\in_1$	0.42×10^{-2}	δ_1	4
ψ_1	1.92×10^{-2}	k_p	0.16
k_i	0.01	k_d	0

The criteria for tuning the parameters of Eqs. (16)–(24) are to obtain the best tradeoff between the minimum desired overshoot and quickest response for position control and stiffness control. Detailed information is listed in Table 3.

3.2. TDE method and PI control

To verify the control performance of the proposed method, the experimental results are compared with TDE and PI control [16,17]. As noted in many previous works, the dynamics of the SMA-actuated system can be expressed in the form of a nonlinear second-order system that can be described as follows:

$$J\ddot{x} + \vartheta\dot{x} + \varphi x + \varsigma = f_3(x, \dot{x}, u) + \omega u \tag{25}$$

where $\ddot{x}$, $\dot{x}$ and x represent the acceleration, velocity and position of the system, respectively; J, ϑ, and φ denote the effective inertia, effective damping and effective stiffness, respectively; ς expresses unexpected disturbances; $f_3(x, \dot{x}, u)$ is the hysteretic nonlinear term; u is the input (applied voltage in this paper); and ω is the input coefficient.

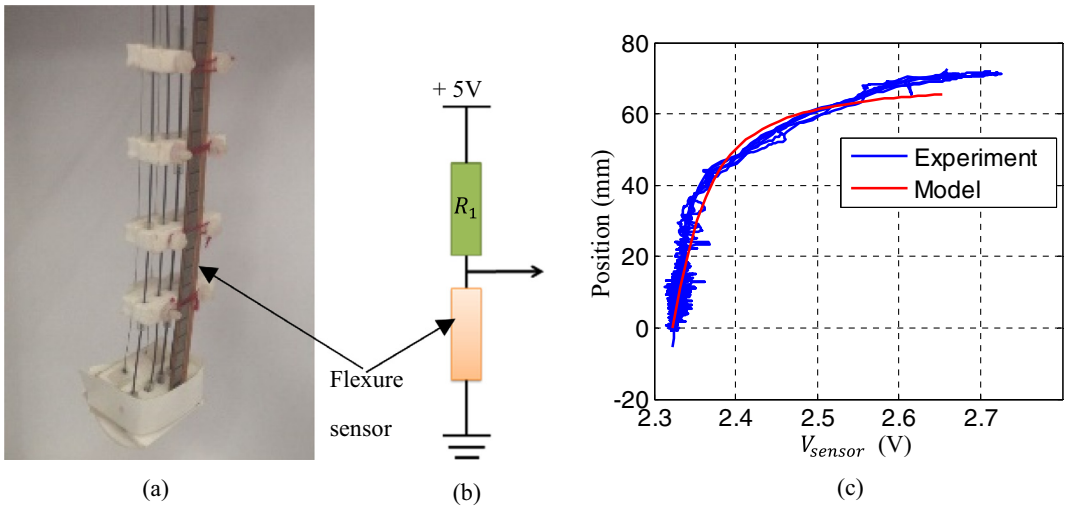

Fig. 6. Position measurement method. (a) Experimental setup; (b) circuit diagram; (c) model and experimental results.

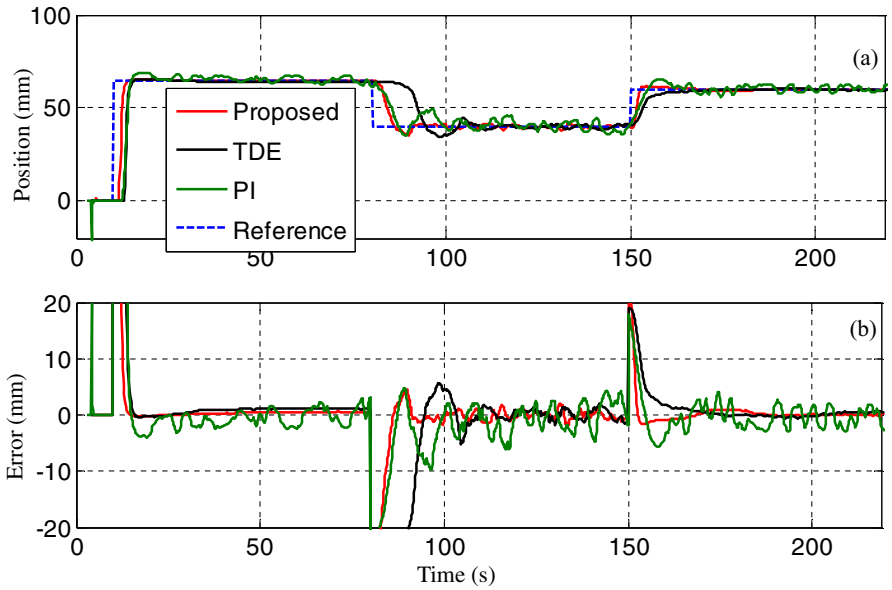

Fig. 7. Position tracking results without variable stiffness for the proposed method, TDE and PI. (a) Tracking performance of point B using a square trajectory and (b) tracking error.

The bending system of the soft robot actuated by SMA-2 can be considered as the second-order dynamics of the system. Then, Eq. (25) can be rewritten as:

$$u = B\ddot{x} + A \tag{26}$$

where $A = [\vartheta\dot{x} + \varphi x + p - f_2(x, \dot{x}, u)]/\omega$ is the total sum of the nonlinearities, frictions and disturbances and $B = J/\omega$ is a control parameter.

Since A is difficult to obtain, TDE can effectively estimate the nonlinearity of the SMA actuator system; the simplified Eq. (26) can be expressed by:

$$u = B\ddot{x} + A \tag{27}$$

Here, A is the estimated A, which can be expressed by:

$$\tilde{A} = A_{t-\mathbb{Z}} \tag{28}$$

where $\mathbb{Z}$ is the time delay.

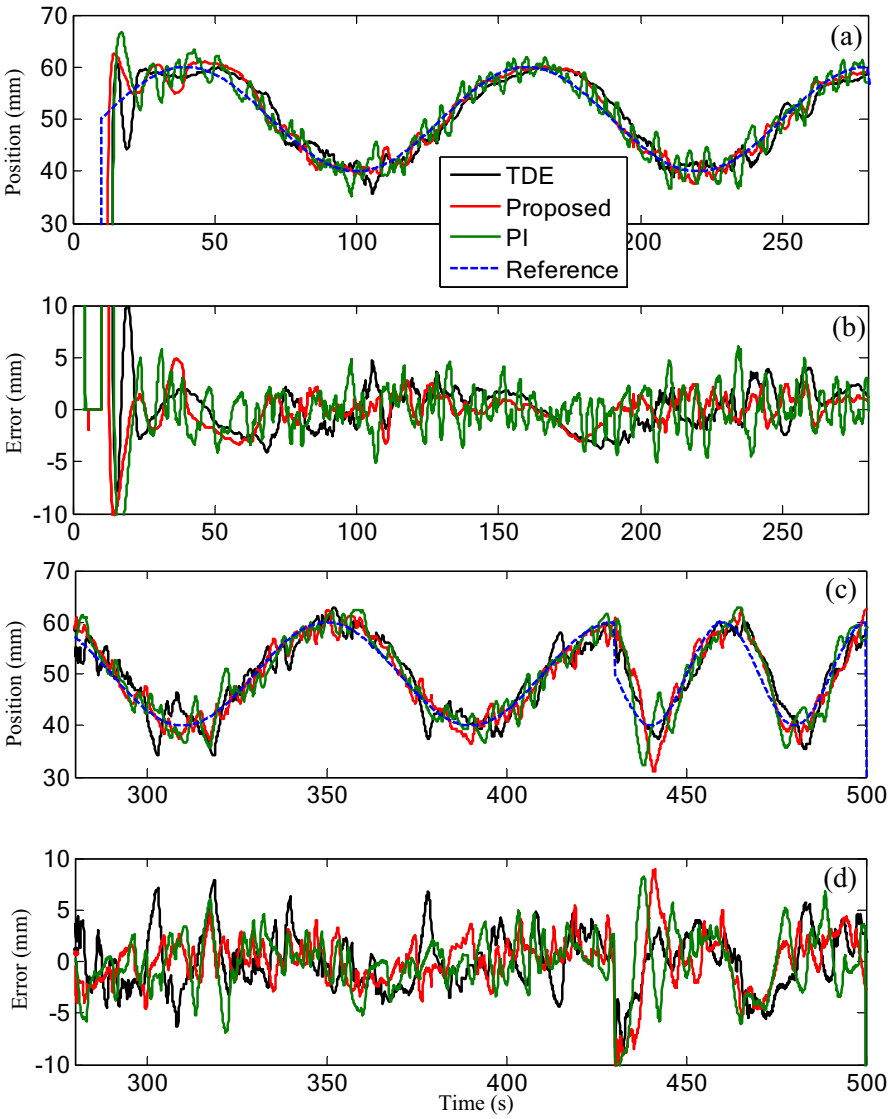

Fig. 8. Position-tracking results without variable stiffness for the proposed method, TDE and PI. (a) Tracking performance of point B using a sine trajectory f = 1/120 Hz; (b) tracking error; (c) f = 1/80 Hz and f = 1/40 Hz; and (d) tracking error.

To achieve the control objective, the assumptions are as follows: (1) the sampling time of the control system is constant and sufficiently small for TDE, and (2) the TDE error $\Gamma = \left|A - \tilde{A}\right| \leq \aleph_2$ is bounded, where $\aleph_2$ denotes a positive value.

Here, to obtain accurate control results, SMC is also added to the control system to achieve the control objective. First, a sliding surface is defined as:

$$s_1(k) = \zeta e(k) + \dot{e}(k), \quad \zeta > 0 \tag{29}$$

where ζ denotes design value.

Then, the reaching law for SMC is chosen as:

$$\dot{s_1} + \lambda s_1 = 0 \tag{30}$$

where λ is a designed positive constant. From Eqs. (29) and (30), the desired closed-loop error dynamics for tracking control is then derived as follows:

$$\ddot{e} + (\lambda + \zeta)\dot{e} + \lambda\zeta e = 0 \tag{31}$$

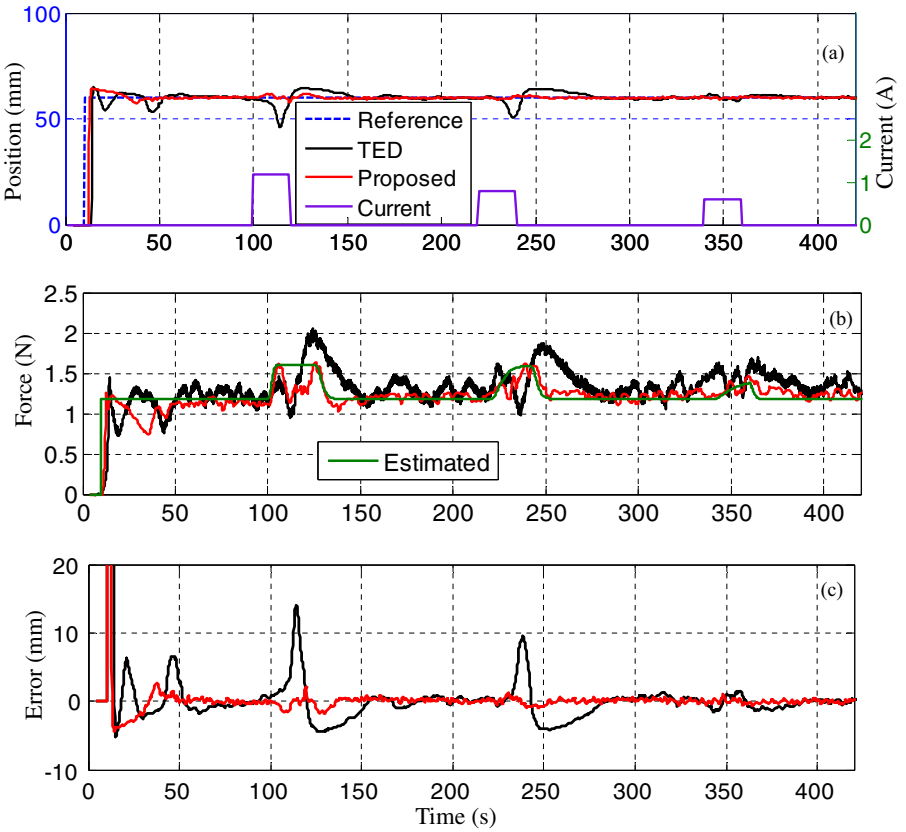

Fig. 9. Position-tracking results with a variable stiffness for the proposed method and TDE. (a) Tracking performance of point B in the X direction for both methods using a step trajectory; (b) estimated and actual bending forces; and (c) tracking error.

Table 4
Error under various control methods.

Error (mm) (maximum/minimum)			
		Proposed	TED
i_{SMA-3}	1.2 A	2.0/−1.8	14.0/−4.3
	0.8 A	1.1/−1.0	9.5/−4.1
	0.6 A	1.0/−0.6	1.5/−1.6
Time	100 s–220 s	5.1/−3.4	7.8/−5.4
	220 s–340 s	5.0/−2.7	12.5/−3.0
	340 s–460 s	4.1/−6.0	8.1/−7.9

Finally, combining Eqs. (26)–(31), the control law can be given as:

$$u = B(\ddot{x}_d + (\lambda + \zeta)\dot{e} + \lambda\zeta e) + u_{t-\mathbb{P}} - B\ddot{x}_{(t-\mathbb{P})} \tag{32}$$

Since the microcontroller sends a PWM value to the driver circuit to control the input voltage of the SM wires, and the microcontroller can receive only PWM values from 0 to 255, the traditional PID controller has the following form:

$$PWM_t = PWM_{t-\mathbb{P}} + k_p e + k_i \int e dt + k_d \dot{e} \tag{33}$$

where $\mathbb{P}$ is the sampling time and k_p, k_i, k_d are the parameters. Detailed information is listed in Table 3.

3.3. Experimental results

To measure the tip position as shown in Fig. 6(a), a flexure sensor is fixed to the soft robot. The resistance of the flexure sensor changes when the soft robot bends, resulting in a variation of its applied voltage. Fig. 6(b) shows the circuit diagram of the flexure sensor, which is connected in series with resistor R_1 =10 kΩ. Voltage V_{sensor} can be measured with

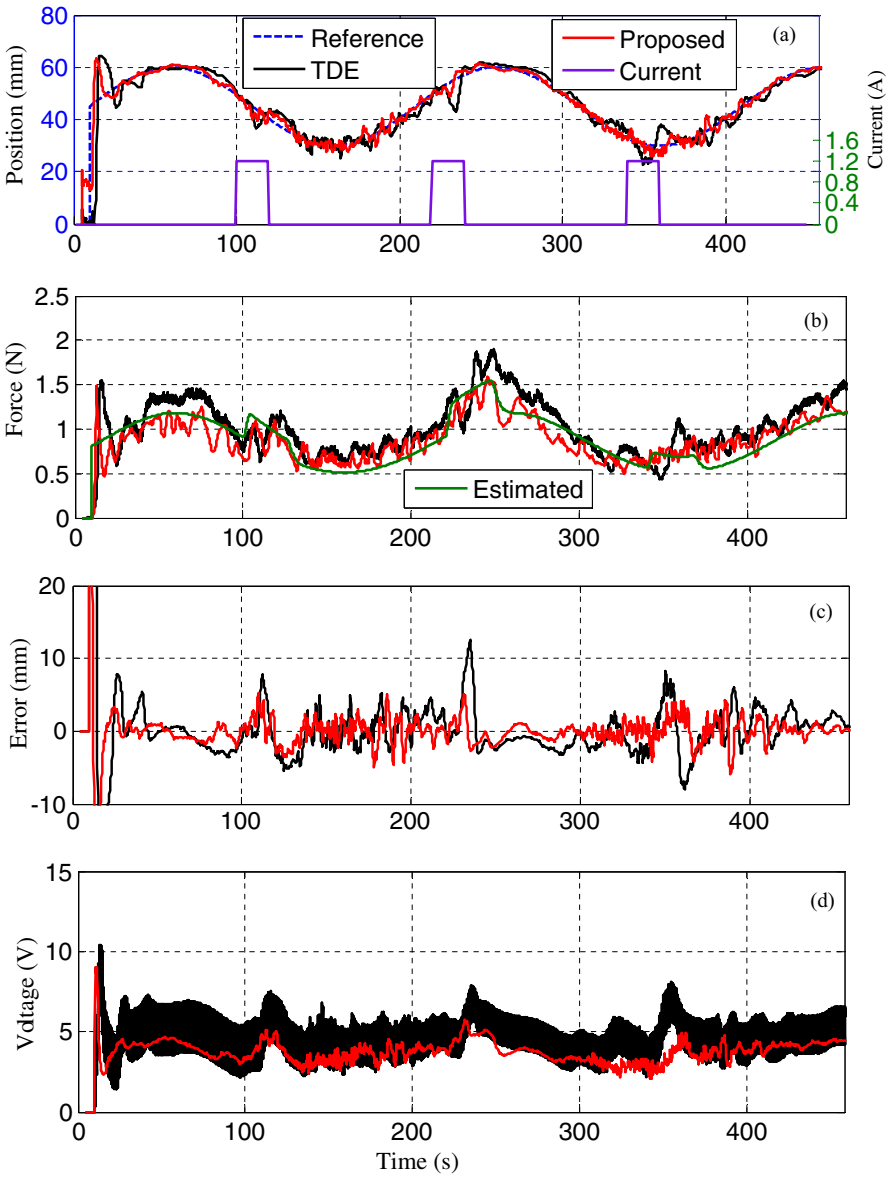

Fig. 10. Position-tracking results with a variable stiffness for the proposed method and TDE. (a) Tracking performance of point B in the X direction for both methods using a sine trajectory with f = 1/200 Hz; (b) estimated and actual bending force; (c) tracking error; and (d) input voltage.

a microcontroller and used to represent the bending position of the soft robot. Voltage V_{sensor} is first normalized, and then its position x can be expressed by:

$$\begin{cases} V_{nor} = (V_{sensor} - V_{min})/(V_{max} - V_{min}) \\ x = \text{atan}(V_{nor}N_1)/N_2 \end{cases} \tag{34}$$

where V_{min} and V_{max} are the minimum and maximum applied voltages of the flexure sensor, respectively; V_{nor} is the normalized value; and N_1 and N_2 are positive coefficients. Fig. 6(c) shows that this simple model expressed in Eq. (34) qualitatively agrees with the experimental results, especially when the position is less than 60 mm. Detailed information is listed in Table 3.

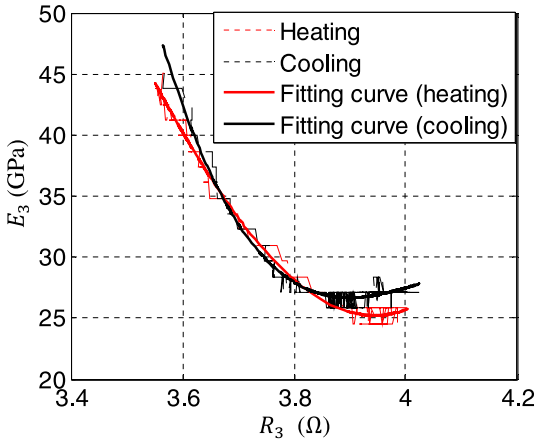

Fig. 11. The relationship between the resistance and the Young's modulus of SMA-3.

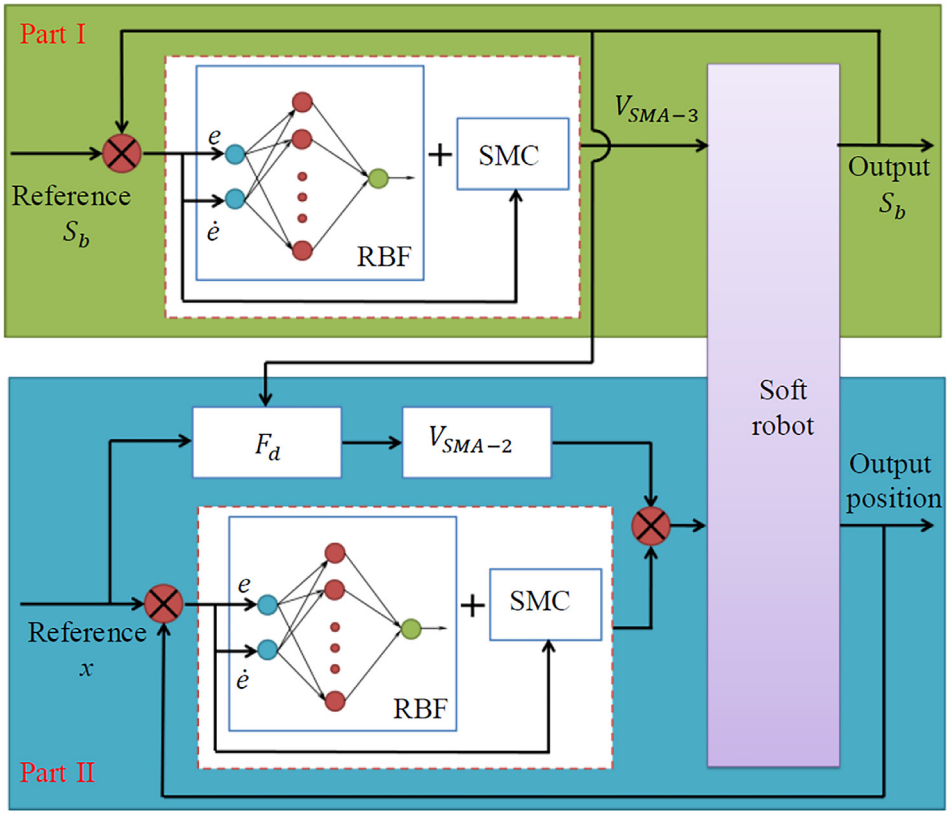

Fig. 12. Position-control strategy of the soft robot under closed-loop stiffness control. Part I is the closed-loop control of stiffness; Part II is position control.

Before position control and variable stiffness control were simultaneously tested, position control was first examined alone to verify the effectiveness of the control strategy. Fig. 7 shows the position-tracking performance for a square command without variable stiffness ($i_{SMA-3} = 0$). As shown in Fig. 7(a), the proposed method demonstrates a faster response speed and fewer oscillations than TDE during heating (10 s to 80 s, 150 s to 220 s and 290 s to 360 s) and cooling (80 s to 150 s and 220 s to 290 s). It is clearer to check the settling time ($e \rightarrow 0$) depicted in Fig. 7(b). For example, the settling times for the proposed method and TDE during the period from 80 s to 150 s are 12 s and 30 s, respectively. The root mean square error is $e_{RMS} = \sqrt{\sum_{j=1}^{k}(e_j^2/k)}$ from 50 s to 320 s for the proposed method, TDE and PI are 3.12, 3.32 and 10.23, respectively. Although TDE is better than the linear PI controller in the position control performance, the result demonstrates that the proposed method has the best performance. Fig. 8 shows the tracking results for a sinusoidal command with a different frequency f. As shown in Fig. 8(a, b), the maximum and minimum errors of the proposed method, TDE and PI during the tracking period from 50 s to 280 s are 2.8 mm and −3.8 mm, 4.8 mm and −3.8 mm, 6.1 mm and −5.1 mm, respectively. The figure clearly shows that the proposed method leads to the smallest tracking error with f = 1/120 Hz. Fig. 8(c, d) show that at higher frequencies f = 1/80 Hz (from 280 s to 430 s) and f = 1/40 Hz (from 430 s to 500 s), the tracking performance is much worse for these control methods. Since the tracking performance of the PI controller at a high frequency is worse than the proposed method and TDE, it is necessary to test the tracking performance under low frequency using the proposed method and TDE to clearly observe the tracking ability of the control method and distinguish the tracking error caused by the changed stiffness.

Fig. 9 shows the position-tracking performance of the step command based on the proposed method and TDE; the stiffness of the soft robot was adjusted simultaneously with the open-loop control system. As shown in Fig. 9(a), the proposed method has a faster tracking speed than TDE when the stiffness remains unchanged from 10 s to 100 s, which is similar to the results shown in Fig. 7. For example, the settling times for the proposed method and TDE from 10 s to 100 s are 40 s and 70 s, respectively. During the variable stiffness process from 100 s to 420 s, "on-off" input current i_{SMA-3} was set with the method shown in Fig. 3. There is a large overshoot and undershoot for TDE when input current i_{SMA-3} was set to 1.2 A to heat the SMA-3 from 100 s to 120 s and cut off from 120 s to 220 s. However, the proposed method leads to many fewer oscillations than does TDE because, as shown in Fig. 9(b), the estimated F_d derived from the proposed model can accurately represent the actual requirement for the bending force when stiffness changes, which can be used to calculate an ideal input voltage for the SMA-2. As shown in Fig. 2(a), the actual bending force of the soft robot is measured by the load cell, which is used to compare with the estimated F_d. All nonlinear effects and tracking errors can be compensated using RBF, which is clarified by checking the errors depicted in Fig. 9(c). The maximum and minimum errors for TDE are 14.0 mm and −4.3 mm, respectively, while the maximum and minimum errors for the proposed method are 2.0 mm and −1.8 mm, respectively.

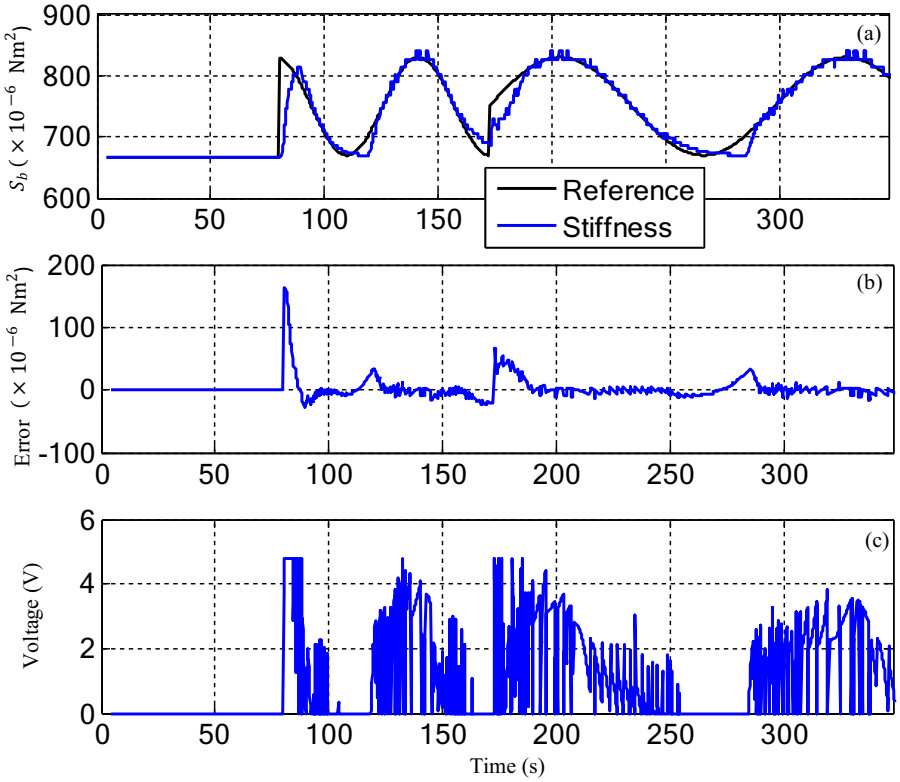

Fig. 13. Stiffness-tracking-control results. (a) Tracking performance for stiffness; (b) tracking error; and (c) input voltage.

Furthermore, the proposed method leads to smaller oscillations than TDE when i_{SMA-3} is set to 0.8 A and 0.6 A to heat the SMA-3 from 220 s to 240 s and from 340 s to 360 s, respectively. The corresponding input voltages are shown in Fig. 9(d), and detailed error information is listed in Table 4.

In the next test, a sinusoidal command was selected as a reference to test the tracking ability and robustness of the proposed method. The trajectory is expressed as:$45 + 15\sin[0.01\pi(t - 10)]$. As shown in Fig. 10(a), the proposed method has a more accurate tracking performance than TDE, especially when i_{SMA-3} is set to 1.2 A to heat the SMA-3 from 100 s to 120 s, 220 s to 240 s and 340 s to 360 s. In addition, as shown in Fig. 10(b), the estimated F_d lines are closer to the experimental results than to those of TDE. Fig. 10(c) clearly shows that the proposed method has smaller tracking errors than TDE. The maximum and minimum errors during the variable stiffness process from 100 s to 220 s, 220 s to 340 s and 340 s to 460 s were 7.8 and −5.4 mm, 12.5 and −3.0 mm, and 8.1 and −7.9 mm, respectively, while these values for the proposed method were 5.1 and −3.4 mm, 5.0 and −2.7 mm, and 4.1 mm and −6.0 mm, respectively. Fig. 10(d) shows the corresponding input voltages; detailed error information is listed in Table 4.

4. Position tracking with closed-loop stiffness control

4.1. Control method design

Section 3 presents the position-tracking performance under open-loop stiffness control, which is not sufficient when the stiffness of the soft robot must be adjusted according to requirements. Since the stiffness of the soft robot cannot be directly

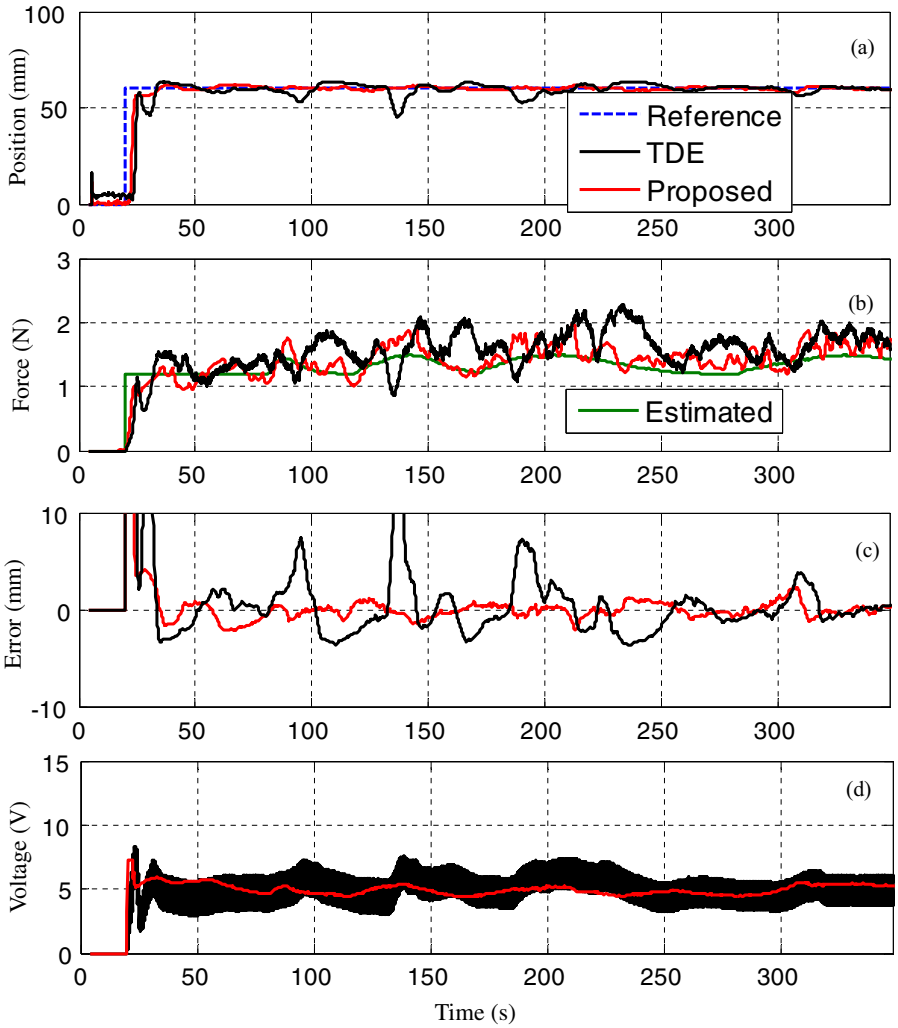

Fig. 14. Position-tracking results with a variable stiffness for the proposed method and TDE. (a) Tracking performance of point B in the x direction for both methods using a step trajectory; (b) estimated bending force and actual bending force; (c) tracking error; and (d) input voltage.

measured using instrumentation, an indirect method must be developed. Therefore, the resistance R_3 of the SMA-3 is used to represent Young's modulus E_3. As shown in Fig. 11, the dashed lines represent the relationship between the resistance R_3 and Young's modulus E_3 for heating and cooling. These experimental results can be fitted and expressed by:

$$E_3 = \begin{cases} z_{h3}R_3^3 + z_{h2}R_3^2 + z_{h1}R_3 + z_{h0} & heating \\ z_{c3}R_3^3 + z_{c2}R_3^2 + z_{c1}R_3 + z_{c0} & cooling \end{cases} \tag{35}$$

where Z_{hj} and Z_{cj} with subscripts j are the fitting parameters.

Then, by combining Eqs. (10) and (35) in a real-time control system, a self-sensing method is established for stiffness. As shown in Fig. 12, Part I demonstrates a hybrid control strategy by combining SMC and RBF (SMC-RBF) to control stiffness, which can be used to predict the bending force of the soft robot.

The control law for the stiffness-control strategy can be expressed as:

$$V_{SMA-3} = \psi_1 W_1^T(k_1)H_1(k_1) + \psi_1 q_1(c_1 e_1(k_1) + \dot{e}_1(k_1))\psi_1 \epsilon_1 sign\{[c_1 e_1(k_1) + \dot{e}_1(k_1)]/\delta_1\} \tag{36}$$

where $e_1(k_1) = S_a(k_1) - S_d(k_1)$ and $\dot{e}_1(k_1) = [e_1(k_1) - e_1(k_1 - 1)]/dt$.$\psi_1$, q_1, c_1, ϵ_1 and δ_1 denote design values; dt is the sampling time of the microcontroller; S_a and S_d are the actual and desired stiffnesses, respectively, and $W_1^T(k_1)H_1(k_1)$ has the same structure as Eq. (15). Part II presents the same position-control strategy that is demonstrated in Fig. (4), while this part will be replaced by Eq. (32) for the TDE method. Detailed parameter information is listed in Table 3.

4.2. Experimental results

A sinusoidal command was selected as a reference to obtain closed-loop control of the stiffness based on SMC-RBF. The trajectory is expressed as:

$$S_d = \begin{cases} 667, & 10 \le t < 80 \\ 750 + 10\ \sin(0.1t), & 80 \le t \le 172 \\ 750 + 100\ \sin[0.05\ (t - 172)], & 172 < t \le 350 \end{cases} \tag{37}$$

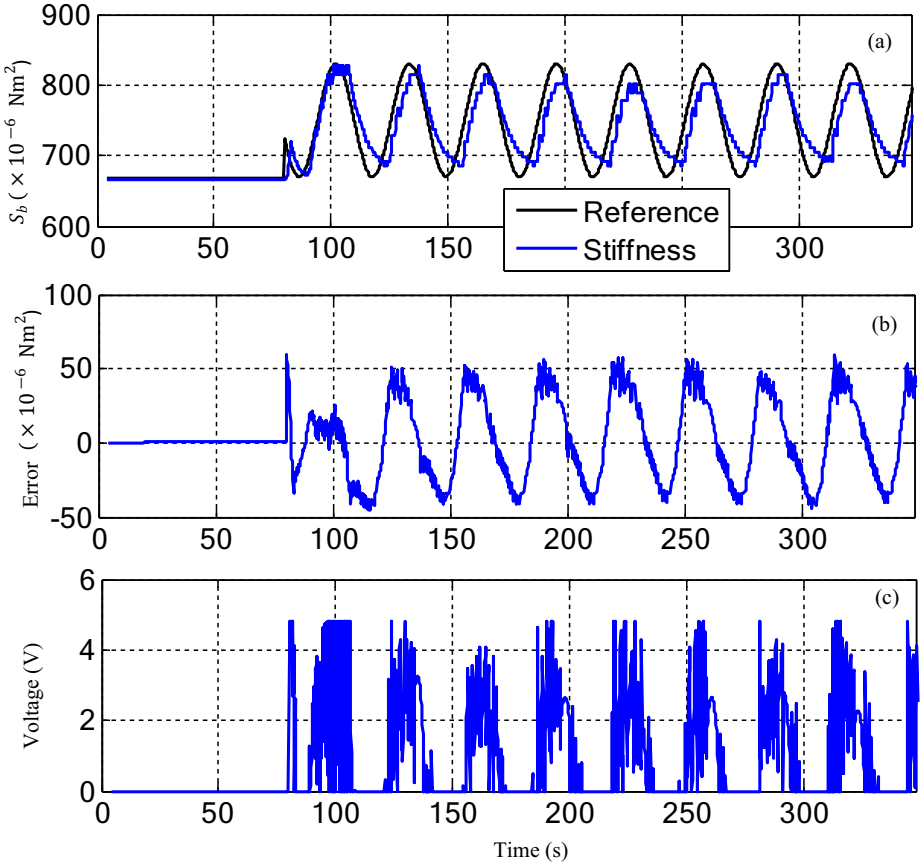

Fig. 15. Stiffness-tracking-control results. (a) Tracking performance for stiffness; (b) tracking error; and (c) input voltage.

Fig. 13(a) clearly demonstrates that stiffness can be adjusted in the closed-loop control system, resulting in good tracking performance based on SMC-RBF. The purpose of the unchanged stiffness from 10 s to 80 s is to obtain stable position-tracking performance, which can ensure more accurate tracking results when stiffness changes during the following process. For example, Fig. 14 shows the position-tracking results with the step command when stiffness is changed according to the reference shown in Fig. 13(a). As shown in Fig. 14(a), the tracking oscillation from 25 s to 35 s results from the control system of the TDE and is not caused by the variable stiffness of the soft robot. Fig. 13(b) and (c) show the corresponding tracking error and input voltage, respectively. In addition, Fig. 14(a) shows that the proposed method leads to more accurate tracking results than TDE. Fig. 14(b) shows that the estimated bending force based on Eqs. (10) and (35) lies closer to the experimental results of the proposed method than to those of TDE, which in turn can explain why the proposed method has fewer oscillations than TDE. Fig. 14(c) clearly shows that the proposed method has a smaller tracking error than TDE, and Fig. 14(d) shows the corresponding input voltages.

To test the tracking ability of the stiffness control method with a higher frequency, the trajectory is expressed as:

$$S_d = \begin{cases} 667, & 10 \le t < 80 \\ 750 + 20\sin(0.2t), & 80 \le t \le 350 \end{cases} \tag{38}$$

As shown in Fig. 15(a), the stiffness of the soft robot remains unchanged from 10 s to 80 s for the reason mentioned in Fig. 13(a). The tracking performance with frequency $f = 1/10\pi$ is much worse than that at lower frequencies, as shown in Fig. 13(a). Fig. 15(b) and (c) show the tracking error and input voltage, respectively. Fig. 16 shows the position-tracking

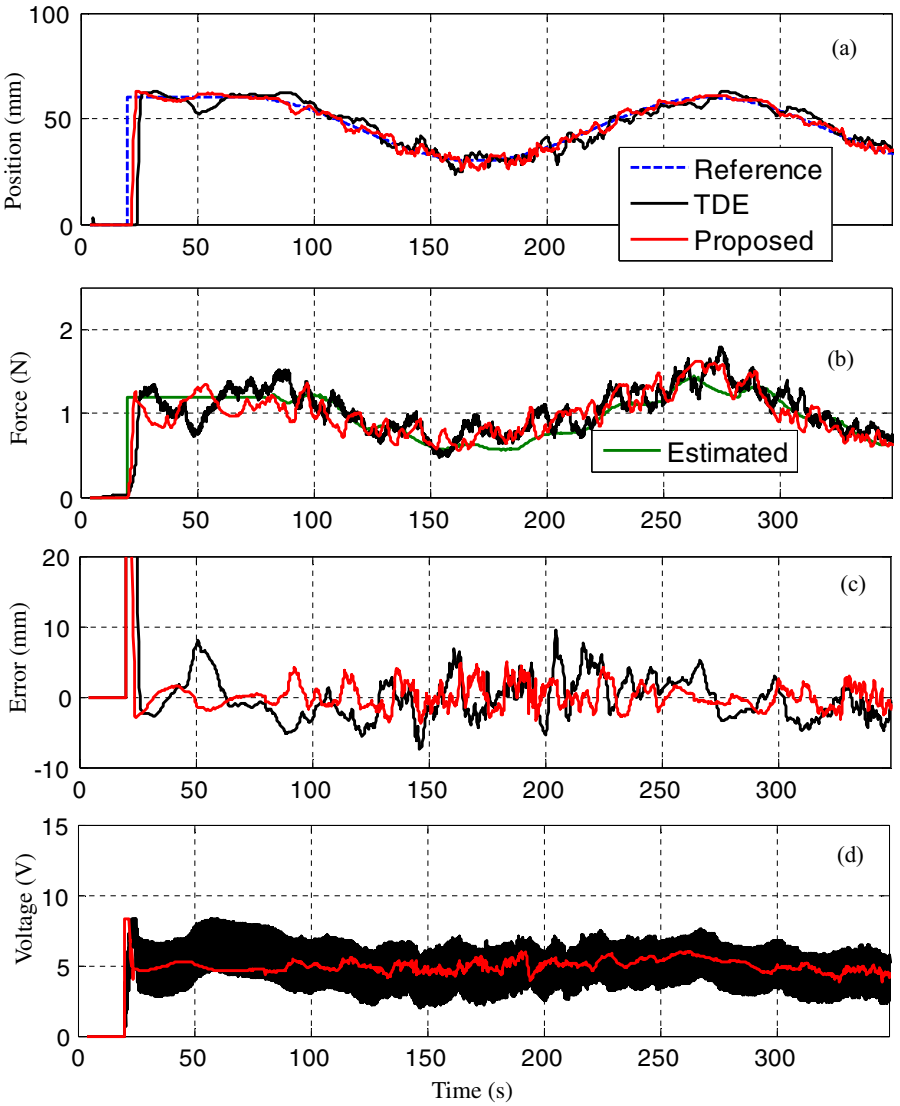

Fig. 16. Position-tracking results with a variable stiffness for the proposed method and TDE. (a) Tracking performance of point B in the x direction for both methods using a sine trajectory with $f = 1/400$ Hz; (b) estimated and actual bending force; (c) tracking error; and (d) input voltage.

results with the sinusoidal command when the stiffness is changed according to the reference shown in Fig. 15(a). As shown in Fig. 16(a), the proposed method still leads to fewer oscillations than TDE, even though the tracking improvement is less obvious when compared with Fig. 14. Fig. 16(b), (c) and (d) show the bending forces, tracking errors and input voltages, respectively.

5. Conclusion

Compared with previous research that has separately focused on the position tracking [2] or stiffness control [7,10] of soft robots, this paper proposes a feasible method to control the position and stiffness simultaneously. A control method is presented based on predicting the bending force and RBF compensation to obtain accurate position-tracking performance when stiffness is simultaneously adjusted in both open- and closed-loop control systems. The experimental results show that the proposed method is more robust than TDE and PI, especially when stiffness is changed dramatically in an open-loop control system. A self-sensing method based on resistance is presented to complete the closed-loop control of the soft robot stiffness, which can be used to predict the bending force in the position-tracking process. The experimental results show that the proposed method based on the predicted bending force leads to better position-tracking results than TDE (without the predicted bending force).

Acknowledgment

This project is supported by National Natural Science Foundation of China (Grant No. 51705382).

References

[1] Xuanming Lu, Weiliang Xu, Xiaoning Li, A soft robotic tongue-mechatronic design and surface reconstruction, IEEE/ASME Trans. Mechatron. 22 (5) (Oct. 2017) 2102–2110.
[2] Jessica Burgner-Kahrs, D. Caleb Rucker, Howie Choset, Continuum robots for medical applications: a survey, IEEE Trans. Robot. 31 (6) (2015) 1261–1280.
[3] Y.J. Kim, S. Cheng, S. Kim, K. Iagnemma, A novel layer jamming mechanism with tunable stiffness capability for minimally invasive surgery, IEEE Trans. Robot. 29 (4) (2013) 1031–1042.
[4] Wei Wang, Hugo Rodrigue, Sung-Hoon Ahn, Smart soft composite actuator with shape retention capability using embedded fusible alloy structures, Compos. B 78 (2015) 507–514.
[5] J. Li, W. Chang, Q. Li, Soft robot with a novel variable friction design actuated by SMA and electromagnet, Smart Mater. Struct. 27 (115020) (2018) 1–11.
[6] D. Josephine Selvarani Ruth, K. Dhanalakshmi, Shape memory alloy wire for self-sensing servo actuation, Mech. Syst. Sig. Process. 83 (2017) 36–52.
[7] Yin Haibin, Kong Cheng, Li Junfeng, Yang Guilin, Modeling of grasping force for a soft robotic gripper with variable stiffness, Mech. Mach. Theory 128 (2018) 254–274.
[8] J. Lee, M. Jin, K.K. Ahn, Precise tracking control of shape memory alloy actuator systems using hyperbolic tangential sliding mode control with time delay estimation, Mechatronics 23 (2013) 310–317.
[9] M. Jin, J. Lee, K.K. Ahn, Continuous nonsingular terminal sliding-Mode control of shape memory alloy actuators using time delay estimation, IEEE/ASME Trans. Mechatron. 20 (2) (Apr. 2015) 899–909.
[10] Junfeng Li, Lei Zu, Guoliang Zhong, Mingchang He, Haibin Yin, Yuegang Tan, Stiffness characteristics of soft finger with embedded SMA fibers, Compos. Struct. 160 (2017) 758–764.
[11] B. Selden, K. Cho, H. Asada, Segmented shape memory alloy actuators using hysteresis loop control, Smart Mater. Struct. 15 (2) (Apr. 2006) 642–652.
[12] Tai, Nguyen Trong, Kyoung Kwan Ahn, A RBF neural network sliding mode controller for SMA actuator, Int. J. Control Autom. Syst. 8 (6) (2010) 1296–1305.
[13] Shichun Yang, Yaoguang Cao, Zhaoxia Peng, Guoguang Wen, Konghui Guo, Distributed formation control of nonholonomic autonomous vehicle via RBF neural network, Mech. Syst. Sig. Process. 87 (2017) 81–95.
[14] Junfeng Li, Huifang Tian, Position control of SMA actuator based on inverse empirical model and SMC-RBF compensation, Mech. Syst. Sig. Process. 108 (2018) 203–215.
[15] Xiangdong Gao, Yuquan Chen, Deyong You, Zhenlin Xiao, Xiaohui Chen, Detection of micro gap weld joint by using magneto-optical imaging and Kalman filtering compensated with RBF neural network, Mech. Syst. Sig. Process. 84 (2017) 570–583.
[16] Miroslav V. Dokic, Peter M. Clarkson, Real-time adaptive filters for time-delay estimation, Mech. Syst. Sig. Process. 6 (5) (1992) 403–418.
[17] Yi Jin, Pyung Hun Chang, Maolin Jin, Dae Gab Gweon, Stability guaranteed time-delay control of manipulators using nonlinear damping and terminal sliding mode, IEEE/ASME Trans. Indus. Electron. 60 (8) (2013) 3304–3317.